



## Optimal microstructural design for high thermal stability of pure FCC metals based on studying effect of twin boundaries character and network of grain boundaries

Alimadadi, Hossein; Fanta, Alice Bastos; Akiyoshi, Ryutaro; Kasama, Takeshi; Rollett, Anthony D.; Somers, Marcel A. J.; Pantleon, Karen

*Published in:*  
Materials & Design

*Link to article, DOI:*  
[10.1016/j.matdes.2018.04.056](https://doi.org/10.1016/j.matdes.2018.04.056)

*Publication date:*  
2018

*Document Version*  
Peer reviewed version

[Link back to DTU Orbit](#)

### *Citation (APA):*

Alimadadi, H., Fanta, A. B., Akiyoshi, R., Kasama, T., Rollett, A. D., Somers, M. A. J., & Pantleon, K. (2018). Optimal microstructural design for high thermal stability of pure FCC metals based on studying effect of twin boundaries character and network of grain boundaries. *Materials & Design*, 151, 60-73. <https://doi.org/10.1016/j.matdes.2018.04.056>

---

### General rights

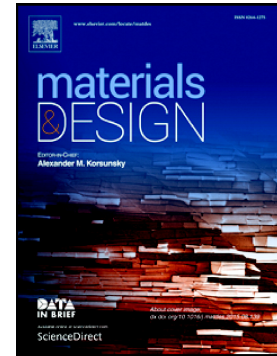
Copyright and moral rights for the publications made accessible in the public portal are retained by the authors and/or other copyright owners and it is a condition of accessing publications that users recognise and abide by the legal requirements associated with these rights.

- Users may download and print one copy of any publication from the public portal for the purpose of private study or research.
- You may not further distribute the material or use it for any profit-making activity or commercial gain
- You may freely distribute the URL identifying the publication in the public portal

If you believe that this document breaches copyright please contact us providing details, and we will remove access to the work immediately and investigate your claim.

## Accepted Manuscript

Optimal microstructural design for high thermal stability of pure FCC metals based on studying effect of twin boundaries character and network of grain boundaries



Hossein Alimadadi, Alice Bastos Fanta, Ryutaro Akiyoshi, Takeshi Kasama, Anthony D. Rollett, Marcel A.J. Somers, Karen Pantleon

PII: S0264-1275(18)30333-2  
DOI: doi:[10.1016/j.matdes.2018.04.056](https://doi.org/10.1016/j.matdes.2018.04.056)  
Reference: JMADE 3869  
To appear in: *Materials & Design*  
Received date: 29 January 2018  
Revised date: 18 April 2018  
Accepted date: 19 April 2018

Please cite this article as: Hossein Alimadadi, Alice Bastos Fanta, Ryutaro Akiyoshi, Takeshi Kasama, Anthony D. Rollett, Marcel A.J. Somers, Karen Pantleon , Optimal microstructural design for high thermal stability of pure FCC metals based on studying effect of twin boundaries character and network of grain boundaries. The address for the corresponding author was captured as affiliation for all authors. Please check if appropriate. *Jmade*(2017), doi:[10.1016/j.matdes.2018.04.056](https://doi.org/10.1016/j.matdes.2018.04.056)

This is a PDF file of an unedited manuscript that has been accepted for publication. As a service to our customers we are providing this early version of the manuscript. The manuscript will undergo copyediting, typesetting, and review of the resulting proof before it is published in its final form. Please note that during the production process errors may be discovered which could affect the content, and all legal disclaimers that apply to the journal pertain.

**Optimal microstructural design for high thermal stability of pure FCC metals based on studying effect of twin boundaries character and network of grain boundaries**

Hossein Alimadadi<sup>1,†</sup>, Alice Bastos Fanta<sup>1</sup>, Ryutaro Akiyoshi<sup>1,2</sup>, Takeshi Kasama<sup>1</sup>, Anthony D. Rollett<sup>3</sup>, Marcel A.J. Somers<sup>4</sup>, Karen Pantleon<sup>4</sup>

<sup>1</sup>Technical University of Denmark, Center for Electron Nanoscopy, Fysikvej, building 307, DK–2800 Kongens Lyngby, Denmark.

<sup>2</sup>Interdisciplinary Graduate School of Engineering Sciences, Kyushu University, 6-1 Kasugakoen, Kasuga, Fukuoka 816-8580, Japan.

<sup>3</sup>Department of Materials Science and Engineering, Carnegie Mellon University, Pittsburgh, PA 15213, USA.

<sup>4</sup>Technical University of Denmark, Department of Mechanical Engineering, Produktionstorvet, building 425, DK – 2800 Kongens Lyngby, Denmark.

† Corresponding Author, E-Mail: hoal@cen.dtu.dk, Tel.: +45 45256494

**Abstract:**

Three nickel electrodeposits with comparable grain size were synthesized by tailoring the electrodeposition conditions. Thorough microstructural characterizations including electron backscatter diffraction, ion channeling contrast imaging, electron channeling contrast imaging, transmission Kikuchi diffraction, transmission electron and high annular dark-field imaging were applied. The deposits contain a high density of twin boundaries with similar microstructures in terms of grain boundary character. These materials were annealed at various temperatures to study the microstructural evolution, and hence, their thermal stability. The differences in the character of twin boundaries and morphology of the grain boundaries in as-deposited state and their influence on the microstructural evolution at elevated temperatures are analyzed. The importance of incoherent twin boundaries, and the interaction of mobile general high angle boundaries with stationary boundaries are discussed. Finally, an optimal design for high thermal stability is proposed, based on the mechanisms that were inferred from the results.

**Keywords:** Thermal Stability, Twin Boundaries, Annealing, Grain Boundary Engineering, Nickel, Electrodeposition

### **1. Introduction:**

More than a half of the overall nickel produced worldwide is used in the form of coatings and nickel electrodeposition is the most common process to coat nickel [1]. High wear resistance, relatively high hardness, barrier properties, corrosion resistance, among others makes nickel electrodeposition of practical importance for a large range of applications [1]. Functional, protective and decorative nickel coatings have been applied in industry [1]. Since thermal stability determines the maximum service time/temperature, it is of high importance for many applications and hence, there is a large body of research on this subject [2]–[8]. The excess free energy of grain boundaries, grain boundary junctions etc. is the major driving force for grain growth in materials [9]–[11]. In order to stabilize the microstructure of nickel electrodeposits, very often alloying with other elements is employed [6], [12]–[18]. The main mechanisms for stabilization is (i) kinetic and (ii) thermodynamic [19]–[21]. In the kinetic approach, the grain boundary mobility is reduced (e.g. solute drag on the boundary motion). In the thermodynamic approach, the driving force for grain growth is reduced by incorporation of a high fraction of low energy boundaries in the microstructure [19]. However, stabilization of pure material has gained interest in recent years [22], [23]. Coherent twin boundaries (CTBs) in face centered cubic (FCC) materials are known to have low mobility [24] combined with low stored energy [25]. Thus, a high density of CTBs in the microstructure should improve the thermal stability of a material [26] due to kinetic and thermodynamic reasons. This has been empirically demonstrated to apply for a nano-twinned microstructure with a high density of CTBs, where improved thermal stability was observed as compared to a nanocrystalline microstructure of equal average crystallite size, but without twins [27], [28]. In addition to the boundary character, the network of grain boundaries plays an important role in the material properties as emphasized in the concept of grain boundary engineering (GBE) [29]–[32]. It is therefore suggested that a GBE microstructure with an abundance of CTBs, is potentially of high

thermal stability. This was demonstrated for nickel deposits, where, among others, multi-twinned grains were observed to have the highest thermal stability [33], [34].

In the present work, it is attempted to elucidate on the mechanism(s) governing the thermal stability of pure FCC nickel electrodeposits with sub-micron grain size and high density of CTBs; and ultimately outline an optimal microstructure to achieve high thermal stability and mechanical strength. To this end, three different nickel electrodeposits with comparable microstructures in terms of grain size and grain boundary character distribution are synthesized and thoroughly studied. Based on the experimental results, the underlying mechanisms of microstructural evolution are identified and an optimal microstructural design for high thermal stability of pure FCC metals is proposed.

## **2. Experimental**

### ***2.1 Materials***

Electrochemical deposition of nickel layers was carried out from a Watts-type electrolyte with the following chemical composition: 300 g.dm<sup>-3</sup> nickel sulfate NiSO<sub>4</sub>·7H<sub>2</sub>O, 35 g.dm<sup>-3</sup> nickel chloride NiCl<sub>2</sub>·6H<sub>2</sub>O, 40 g.dm<sup>-3</sup> boric acid H<sub>3</sub>BO<sub>3</sub>. Nickel was electrodeposited from the electrolyte onto amorphous Ni-P substrates for three different combinations of pH and current density (see Table 1). The pH of the electrolyte was adjusted to the intended value by addition of sulfuric acid or ammonia. Further details of the synthesis parameters are provided elsewhere [35], [36].

To study the thermal stability of the material, the as-deposited samples were cut into smaller pieces of 10×5 mm<sup>2</sup>. They were annealed for 30 min at 473, 573, 673 and 873 K followed by cooling in air. Annealing at 473 K and 573 K was performed in air while argon was used for annealing at 673 K and 873 K, as at higher temperatures oxidation can be more pronounced. Never the less, it was verified that annealing in air and argon for the present temperature and time ranges has the

same influence on the grain growth. The annealed samples are named with a postfix of temperature to the as-deposited sample name. For instance, S1-473 refers to sample S1, annealed at 473 K.

It is worth mentioning that the annealing temperature range of 473 – 873 K corresponds to homologous temperature range of 0.27 – 0.50 for nickel. This homologous temperature range is chosen as for iron and nickel below 0.3 the microstructural evolution is very limited and substantial grain growth takes place at 0.4 [37].

## **2.2 Sample preparation for microscopy**

Electron backscatter diffraction (EBSD) and electron/ion channeling contrast imaging (ECCI/ ICCI) were used to investigate the entire cross-sections in each deposit. This enabled to characterize the evolution of the microstructure along the growth direction (GD). Cross-sections of the samples for scanning electron and ion microscopy were prepared by grinding on SiC paper of grade 1000 and 4000, followed by mechanical polishing with 3  $\mu\text{m}$  and 1  $\mu\text{m}$  diamond suspension, followed by mechanical-chemical polishing with 0.04  $\mu\text{m}$  colloidal silica. To ensure that the deformed layer introduced by mechanical polishing was entirely removed, the samples were milled with a focused ion beam (FIB) of  $\text{Ga}^+$  ions at 30 kV in an FEI Helios NanoLab<sup>TM</sup> 600 dual beam microscope. FIB milling was carried out in two steps: firstly about 700 nm were removed applying a current of 2.8 nA (rough milling), and then an additional 50 nm were removed by milling with a current of 0.46 nA (gentle milling). This sample preparation provided an artifact-free surface that is suitable for surface sensitive characterization techniques such as EBSD [38].

For transmission electron microscopy, an electron transparent foil was prepared in a FEI Helios Nanolab<sup>TM</sup> 600 dual beam microscope, using an in-situ lift-out technique [39], in which 30 kV  $\text{Ga}^+$  were used for the penultimate step. For the final step (removal of amorphous layer), 2 kV  $\text{Ga}^+$  with a current of 6 pA was applied with an incident angle of  $7^\circ$  to both sides of the foil for 10 min. The foil covers the whole thickness of the deposit and contains the GD within the plane of the foil.

### 2.3 EBSD

**Data Acquisition:** To examine the character of the grain boundaries and their connectivity, orientation mapping was performed in an FEI Helios NanoLab<sup>TM</sup> 600 equipped with an EDAX-TSL EBSD system. The EBSD measurements were carried out on a hexagonal grid with an electron probe current of 5.5 nA at an acceleration voltage of 12 kV and a step size of 25 nm.

**Data Analysis:** The OIM 6<sup>TM</sup> software was used for the analysis of the acquired EBSD data. Post-acquisition treatment of the recorded EBSD data included the following cleaning steps using routines available in the OIM 6<sup>TM</sup> software. Firstly, the confidence index (CI) [40] of every point in the map within a recognized grain was assigned to the highest confidence index CI value found in that grain (a grain was defined as a region consisting of at least three connected points with misorientation of less than 5°). Secondly, by so-called grain dilation, a point with an orientation that does not belong to any grain is assigned the orientation of the majority of neighboring points. Afterwards, all data points with CI below 0.1 were disregarded. It is noted that the cleaning procedure mainly discards the measured data points outside the deposit area (substrate and beyond the top surface) and has a very limited effect on the actual area of interest, namely, just assigning correct orientations to the mis-indexed data points at the grain boundaries.

**Substrate/deposit interface definition:** Since the grain size in the bottom part of the deposit, i.e., adjacent to the substrate, is smaller than the EBSD resolution [41], it is essential to define the position of the substrate/deposit interface for the EBSD investigations. To accomplish this, the CI value of the as-measured data (before any cleaning) was averaged for all the points with the same distance from the bottom of the map. Since the substrate was amorphous the line average CI was 0. The location of the interface was taken as the location where the average CI exceeds 0.1 (see details in [41]). For studying the evolution of the microstructure with distance from the substrate/deposit

interface, the EBSD map was subdivided in sub-maps of 2  $\mu\text{m}$  width from the position of the defined interface to the surface.

**Grain boundary character:** In order to examine the grain boundary character the following parameters were calculated for each 2- $\mu\text{m}$ -sub-map: (i) the average intercept length was obtained by passing 3 horizontal lines through the sub-map; any pair of points with a point-to-point misorientation larger than  $15^\circ$  were taken to be an intercept; (ii) the length fraction of low angle grain boundaries (LAGB), i.e., point-to-point misorientations between  $2^\circ$ –  $15^\circ$ ; (iii) the length fraction of high angle grain boundaries (HAGB) having a point-to-point misorientation in the range  $15^\circ$ –  $62.8^\circ$ ; (iv) the length fraction of  $\Sigma 3$  and  $\Sigma 9$  boundaries identified according to Brandon's criterion [42].

**Grain boundary network:** In order to characterize the connectivity/fragmentation of the HAGB network by  $\Sigma 3^n$  boundaries, black and white images of non- $\Sigma 3^n$  ( $n=1,2$  and  $3$ ) HAGBs were made. Homology metrics, known in the topology literature as Betti numbers [43],  $B_0$  and  $B_1$ , were calculated, using the software CHomP [44], [45]. The scale invariant ratio of  $B_0/B_1$ , hereafter  $\beta_{01}$ , which is the inverse of connectivity [46], is calculated for each sub-map.

#### **2.4 Electron/Ion channeling contrast imaging**

The prepared cross sections of the samples were investigated with ECCI and ICCI in the same microscope mentioned in section 2.2. ECCI was applied prior to EBSD measurements using an accelerating voltage of 10 kV and a probe current of 1.4 nA. ICCI was applied as a complementary mapping to EBSD [47] using the FIB operated at 30 kV; the applied probe current was chosen to minimize the risk for ion-beam induced changes to the microstructure. To this end, the applied probe current was optimized for each sample (ion doses ranging from  $0.5$  –  $4.3 \text{ C m}^{-2}$  were applied). ICCI was always carried out as the final investigation, i.e., after EBSD had been carried out over the same area of the sample [47].

## 2.5 Transmission electron microscopy

**High Voltage:** Scanning transmission electron microscopy (STEM) investigations were carried out at 300 kV in an FEI Titan 80-300ST field emission gun TEM equipped with a Fischione high-angle annular dark-field detector and a Gatan bright-field detector located at the entrance of a Gatan imaging filter. In order to characterize twin related grains, a double tilt specimen holder was utilized to align the common  $\langle 110 \rangle$  direction of the twin-related grains parallel to the incoming electron beam.

**Low Voltage:** Transmission Kikuchi diffraction (TKD) mapped orientations in the TEM foils before and after annealing at 673 K in vacuum. This was carried out in a FEI Nova NanoLab<sup>TM</sup> 600 field-emission gun SEM equipped with an EBSD system from Bruker that has an eFlash<sup>HR</sup> camera (Bruker Nano GmbH). The TKD measurement was performed in a  $10 \text{ nm} \times 10 \text{ nm}$  square grid with an electron probe current of 4.9 nA at an acceleration voltage of 30 kV. The TKD maps were analyzed with Esprit 2.0 software from Bruker.

## 3. Results

### 3.1 Microstructure of as-deposited state

The EBSD orientation maps covering the whole cross section of the samples in the as-deposited state are shown in Fig. 1 (HAGBs are marked in black). All three samples have columnar microstructure. Very fine grains are present in the vicinity of the deposit/substrate interface and columnar grains develop from these fine grains away from the substrate. In the inverse pole figure color coding scheme used for Fig. 1, the major crystallographic orientations correspond to  $\langle 211 \rangle$ ,  $\langle 100 \rangle$  and  $\langle 210 \rangle$  parallel to the GD for samples S1, S2 and S3 respectively. The details of the texture and orientation relations were previously provided elsewhere [35], [36], hence, are not repeated here.

### 3.2 Grain size of as-deposited state

The ICCI micrographs shown in Fig. 2 have higher spatial resolution as compared to the EBSD results [48]. Thus, it is advantageous to use ICCI for grain size characterization in the as-deposited state, especially for the nanocrystalline regions. Additional micrographs at higher magnification were also made to resolve the nanocrystalline regions (see, for example, Fig. 2d for sample S3). The black and white images were processed using the Canny edge detection algorithm [49]. Based on the length of horizontal line and the number of intercepts, the average horizontal intercept length (AHIL) was calculated. Finally a square root function which accurately describes the increase of grain width (within the plane of the deposit) in the GD [50], was fitted to the data points (Fig. 3). Further details were provided elsewhere [51].

### ***3.3 Grain boundary character of as-deposited state***

Using the EBSD data behind the orientation maps of Fig. 1, the grain boundaries' character and their evolution with increase of deposit thickness were analyzed. Specifically, the length fraction of  $\Sigma 1$  (LAGBs),  $\Sigma 3$ , and  $\Sigma 9$  boundaries, as well as the total percentage of these boundaries are characterized (Fig. 4).

For sample S1 about 90 % of boundaries are HAGBs and about 10 % are LAGBs, independent of distance from the deposit/substrate interface.  $\Sigma 9$  is not of high importance in this sample. The most important boundary is  $\Sigma 3$ . At about 7  $\mu\text{m}$  from the interface, more than 50 % of the boundaries are of  $\Sigma 3$  character. Since the twin lamellae width can amount to 20 nm or less, some of them are overlooked by EBSD, as discussed in depth elsewhere [52]. Thus, the reported  $\Sigma 3$  length fraction is the lower bound.

For sample S2, after the first 2  $\mu\text{m}$ , the boundary character does not change significantly, and the fractions of  $\Sigma 1$ ,  $\Sigma 3$  and  $\Sigma 9$  are 18 %, 33 % and 5 %, respectively. In this sample the  $\Sigma 3$  length fraction is lower than actual value. This is explained in more details in section 4.

For sample S3, about 88 % of boundaries are HAGB and about 12 % are LAGB, independent of distance from the deposit/substrate interface. There is a two-fold increase in length fraction of  $\Sigma 3$  boundaries from 22 % to 44 % in the first 4  $\mu\text{m}$  of the deposit (Fig. 4). Afterwards, there is gradual increase of  $\Sigma 3$  boundaries fraction to 55 %. The  $\Sigma 9$  boundary fraction is about 8 % across the deposit. This value is slightly higher than the actual value, as discussed in depth elsewhere [36].

### ***3.4 Morphology of the twin boundaries in as-deposited state***

The twins in sample S1 are in the form of thin lamellae of a few tens of nanometers in width, elongated along the GD, see Fig. 5a. Observing the microstructure in GD (Fig. 5b) clearly shows that the twin lamellae span the entire width of each columnar grain. Thus they have the 3D morphology shown in Fig. 5c.

Fig. 2b shows that the twins in sample S2 are mostly inclined with respect to GD and span the columnar grains encompassing them. In order to characterize the 3-dimensional configuration of these twin lamellae, serial sectioning and ICCI were applied. A sequence of 6 micrographs with an average distance of 70 nm between the sections is shown in Fig. 6. Two twin lamellae are marked by red and green dots. Since the lamella marked by the green dot is absent in section No.6, and the lamella marked by the red dot is absent in section No.1, these twins evidently terminate within the columnar grain. Additionally 2D micrographs of each section show that the width of the lamellae changes, indicating that the twin boundary plane is stepped and generally has an incoherent component.

The microstructure of sample S3 is the result of stacking of tetrahedra bounded by  $\{111\}$  planes (twin boundary planes) that develop a helical structure [53], according to the scheme shown in Fig. 7a and b. A cross section of such a column along an arbitrary plane shows the patterns revealed in Fig. 7c and corresponds to the features observed in ICCI (Fig. 2c and d). The tetrahedra share  $\{111\}$

planes can be considered to be members of twin-related helices that are columns composed of five-fold twin boundary junctions and a high fraction of  $\Sigma 3$  boundaries [36].

### 3.5 Microstructural evolution upon annealing

Samples annealed at 473 K show very limited growth in the immediate vicinity of the substrate (i.e., the nanocrystalline part of microstructure), so no further analysis was performed for this temperature.

Fig. 8 a–c show ICCI micrographs of samples annealed at 673 K. The orientation maps of the samples after annealing at 873 K are also shown in Figs. 8 d–f. The microstructure of sample S1 is still columnar even after annealing at 873 K. In general, a large fraction of the microstructure corresponds to  $\langle 211 \rangle // \text{GD}$  oriented grains (colored purple in the map) encompassing twin lamellae, similar to the as-deposited state. In the vicinity of the film/substrate interface, significant grain growth took place whereas away from the substrate, the grain growth during annealing is notably less pronounced. The grains near the substrate are equiaxed and their orientation is mainly  $\langle 100 \rangle // \text{GD}$  (colored in red in the orientation map).

The microstructure of sample S2 is also still columnar and resembles the as-deposited state after annealing at 673 K (Fig. 8b). However, after annealing at 873 K notable growth has occurred (Fig. 8e). The growth close to the deposit/substrate interface results in formation of equiaxed grains, while away from the interface, the growth manifested as column widening.

Fig. 8c is a montage of four micrographs from sample S3 after annealing at 673 K. It is evident that local grain growth occurred, close to, but not directly adjacent to the substrate, whereas no further growth appeared for the grains in contact with the substrate. The grain growth is substantial and resemblance to the as-deposited state is lost in this part of the deposit. In regions  $> 5 \mu\text{m}$  from the substrate, larger grains replaced the original structure, indicating that grain growth took place, but also remnants of the original columns, consisting of five-fold multi-twinned regions, are present.

The orientation map obtained after annealing at 873 K is shown in Fig. 8f. Evidently, substantial grain growth occurred such that the five-fold multi-twins of the as-deposited state disappeared and were replaced by large equiaxed grains containing typical annealing twins.

Evidently, sample S3 is significantly less thermally stable than the other two samples and its grain size is about an order of magnitude larger than for the other samples after annealing at 873 K. Thus, it is of interest to analyze in more detail the as-deposited state of sample S3 and its evolution upon annealing, which is provided below in section 3.6.

### ***Evolution of twin boundaries upon annealing***

Typical twin lamellae in  $\langle 211 \rangle // \text{GD}$  oriented grains of sample S1 (parallel to the film GD) were also observed after annealing at 673 and 873 K. This shows that twin lamellae are stable in this configuration. Analyzing ion channeling images of sample S1 showed that the twin lamella frequency is  $\sim 3.5$  per grain which changes after annealing at 873 K to  $\sim 3.1$  per grain (based on a micrograph of  $\approx 25 \mu\text{m} \times 20 \mu\text{m}$ ). For sample S2, most of the twin lamellae within the columnar grains were annihilated after annealing at 873 K. Further quantification shows that 80 % of the twin lamellae were lost. Finally for sample S3 the microstructural evolution is so drastic that a comparison between the as-deposited state and after annealing at 873 is not reasonable. Specifically, none of the growth twins observed in the as-deposited state survived and only annealing twins are present in the microstructure after annealing.

### ***3.6 Detailed characterization of Sample S3***

#### ***As-deposited state***

Fig. 9a shows a low magnification bright field (BF) STEM micrograph of the as-deposited condition of sample S3. Fig. 9b-d show annular dark field (ADF) STEM images of the three locations marked in Fig. 9a by numbers 1, 2 and 3. High resolution investigations reveal that the

majority of the boundaries forming the five-fold structure are actually coherent twin boundaries (Figs. 9b-d). Five twin boundaries do not meet exactly in a single point; instead the five crystallites meet in three-fold and four-fold junctions separated by 2-3 atomic columns. Furthermore, some jogs on the twin boundary planes (shown by arrows in Fig. 9c) were observed and stacking faults may be present adjacent to the twin boundary (see Fig. 9d). An electron diffraction pattern of the five crystallites shown in Fig. 9b is presented in Fig. 9e, showing the approximately five-fold symmetry. Because the presence of a LAGB in addition to the five twin boundaries, two diffraction spots separated by  $5.4^\circ$  are visible (marked with a grey circle in Fig. 9e). A LAGB can be seen as an array of dark contrast in the BF STEM image shown in Fig. 9f. The BF STEM micrographs (Figs. 9f and g) also reveal strain fields. A more detailed BF STEM image of the grain comprising strain fields (darker contrast) in Fig. 9f is shown in Fig. 9g (note that Fig. 9g is obtained from the location just above Fig. 9f). The corresponding Fourier-filtered image of the area enclosed by a white square in Fig. 9g is shown as an inset on the figure and reveals an array of dislocations [54]. In addition to the dislocations' strain fields, a strong strain field is also observed at the grain boundary junction (seen as darker contrast in Fig. 9f).

Five crystals that are related by coherent twins span a total angle of  $352.6^\circ$ , i.e., there is a deficit of  $7.4^\circ$  from a full rotation. Thus, independent of the junction configuration (i.e., a five-fold junction, or a connected pair of 3 fold junctions, etc.) a set of five twins cannot fill space. Consequently, there is an inherent strain associated with five grains related by twinning (see Fig. 9f). Five-fold junctions with elastic accommodation of the misfit have been reported for nano-particles, but for particles larger than several nanometers, disclinations develop to accommodate the misfit between five  $\Sigma 3$  boundaries and a full  $360^\circ$  revolution (see the review in [55]). Such disclinations decompose leaving defects as stacking faults and dislocations, surrounded by strain fields as well as the subdivision of five-fold junctions into junctions of lower order (three- and four-fold) [55].

In addition to the grain boundary character, the network of grain boundaries is of importance in sample S3. For Non- $\Sigma 3^n$  HAGB, the inverse of connectivity ( $\beta_{01}$ ) significantly increases with distance from the substrate. For the consecutive 4  $\mu\text{m}$  wide sub-maps  $\beta_{01}$  is 0.4, 6.6, 11.2 and 22.1. This means that the network of Non- $\Sigma 3^n$  HAGB becomes more and more fragmented as the nickel deposit thickness increases. Note that at the edges of the sub-maps, the grain boundary network is strongly fragmented. Hence, sub-maps with smaller width have larger values of  $\beta_{01}$ . To overcome this shortcoming, a sub-map width of 4  $\mu\text{m}$ , instead of 2  $\mu\text{m}$ , was chosen for characterization of the grain boundary network connectivity.

### *Annealing*

We observed experimentally straight plane traces along CTBs (Fig. 10) in the early stages of grain growth. Fig. 10a shows a typical microstructural feature of the multiply twinned grains (cf. Fig. 10a and Fig. 2d). After annealing at 573 K for 30 min, the microstructure was imaged using ECCI (Fig. 10b). Though the imaged location in Fig. 10b is not identical to that in Fig. 10a, it is apparent that an originally straight twin boundary became curved during annealing. One may argue that the curvature of the boundary detected in Figs. 10b was present in the as-deposited state and is not a result of annealing. In order to rule out this possibility, a thin foil from the nickel deposit was annealed at 673 K in vacuum, and analyzed before and after annealing using TKD at the same location. The comparison between image quality maps before (Fig. 10c) and after annealing (Fig. 10d) clearly shows the grain boundary evolution. One of the twin boundaries is marked before annealing (Fig. 10c) and the same boundary after annealing is curved (Fig. 10d).

Fig. 10e shows the grain boundary map of sample S3 after annealing at 673 K, in which the  $\Sigma 3$ ,  $\Sigma 9$  and general HAGBs (g-HAGBs) are marked in green, blue and red, respectively. Curved  $\Sigma 3$  boundaries are apparent and two of those are marked by green arrows in Fig. 10e. Note that

advancing grain boundaries that border coarsened areas (a few are marked with red arrows) are non- $\Sigma 3^n$  HAGBs.

#### **4. Discussion:**

The three studied electrodeposits are very similar in terms of their columnar microstructure where the columns are repeatedly interrupted by twin boundaries. The fractions of  $\Sigma 3$  boundaries in S1 and S3 are also comparable, whereas a lower fraction was measured for S2 (see Fig. 4). EBSD data is routinely used to characterize grain boundary character; however the spatial resolution of the technique is inadequate in the nanocrystalline regions of the microstructures. Additionally, the spatial resolution of EBSD is asymmetrical because of specimen tilt [56]; hence, inclined twin lamellae in sample S2 are easily overlooked in orientation maps obtained by EBSD (see Fig. 11) as compared to samples S1 and S3 (see further details in [57]). Thus, the actual  $\Sigma 3$  fraction is likely to be higher than what is reported in Fig. 4 for sample S2 and probably comparable with samples S1 and S3 (as estimated by ICCI micrographs). Thus, one might expect a similar microstructural evolution upon annealing, hence, similar thermal stability. However, the only similarity between the microstructural evolution of these samples is the grain growth of the nanocrystalline part of the microstructure at the immediate vicinity of the substrate, which starts at low temperatures. In this region, the grain size is finest compared to the rest of the microstructure in the as-deposited state; hence, the interfacial area per unit volume is largest and this region is more susceptible to grain growth. The grain growth of nanocrystalline material is beyond the scope of this communication because it is not considered to have a major influence on the thermal stability of the columnar part of the electrodeposits.

Fig. 8 shows that these samples respond very differently to annealing. There is high, medium and no resemblance between the as-deposited and annealed states for samples S1, S2 and S3, respectively. Optimal microstructural design for high thermal stability can be highly facilitated if

the underlying mechanism(s) of microstructural evolution in these samples is outlined. To this end, the differences between these samples must be recognized. XRD texture analysis revealed that after annealing, the texture does not notably change compared to the as-deposited state. This is visually evident from the orientation maps for sample S1 and S2 in Fig. 8 (see the results in [51]). This strongly suggested that the difference in thermal stability is not correlated with the as-deposited texture and other parameters are of higher importance. The two major distinguishing and influencing parameters are: (i) The plane of  $\Sigma 3$  boundaries is not identical. In sample S2 the twin boundaries have a higher density of steps than in samples S1 and S3. (ii) Samples S1 and S2 have a columnar microstructure wherein the columnar grain boundaries have no special character, whereas S3 has  $\langle 210 \rangle // \text{GD}$  columns separated from their twin related grains ( $\langle 542 \rangle // \text{GD}$ ) by twin boundaries (see Fig. 1c and [58]).

#### ***4.1 The effect of the twin boundary plane***

Coherent twin boundaries (CTBs) and incoherent twin boundaries (ITBs) both have a  $60^\circ / \langle 111 \rangle$  disorientation ( $\Sigma 3$  in the CSL model [42]). The only difference between the CTBs and ITBs is the plane of the boundary. While the CTB has a boundary plane of  $\{111\}$  type, the ITB has a plane different from  $\{111\}$ . The energy of an ITB is significantly (orders of magnitude) larger than the energy of a CTB and in the same range as for general HAGBs [25]. More importantly, it has been shown for nickel that ITBs have a higher mobility than CTBs [59]: depending on the type of ITB, they can move two orders of magnitude faster than other HAGBs [24]. Accordingly, it is expected that twin boundaries with an incoherent component contribute to grain growth at elevated temperatures. This follows from comparing the thermal stabilities of samples S1 and S2. Both samples are composed of columnar grains separated by high angle grain boundaries with encompassed twin boundaries within the columnar grains. The higher fraction of ITBs in sample S2 accelerates the microstructural evolution during annealing. In this regard, one must take into

account not only the character of boundaries in the as-deposited state but also the evolution of boundaries at elevated temperatures. For sample S3, straight twin boundaries become curved (see Fig. 10). This means that the CTBs evolve into ITBs. The most reasonable rationalization is that the increase in stored energy by transformation of CTBs into ITBs is driven by a reduction of the energy stored in the strain fields and structural faults, such as dislocations, present in the five-fold twinned structures (see Fig. 9). Thus in sample S3 the formation of ITBs accelerates microstructural evolution and is responsible for the poor thermal stability.

#### **4.2 The effect of columnar grain boundary character**

For sample S3 upon annealing at 673 K, grain growth is most pronounced at some distance from the substrate. Evidently, the location where pronounced grain growth is observed at 673 K (see Fig. 10e) coincides with the location from where, in the as-deposited state, multiple twin-related texture components have developed, leading to the high density of  $\Sigma 3$  boundaries (Fig. 4) and multi-twin junctions (see S210 in Fig. 4 in [60]). Perhaps the twin boundaries are stable, but the five-fold junctions are unstable. However, it has been shown that in FCC materials these junctions are relatively stable [61]. High thermal stability is reported, specifically for nickel electrodeposits with a  $\langle 110 \rangle$  fiber texture and five-fold twin boundary junctions [33], [34] which are encompassed by g-HAGB forming isolated units (unlike sample S3 which has a connected helical structure of five-fold junctions). Therefore, to understand the poor thermal stability, the dynamics of grain boundary interaction and the effect of connectivity of the grain boundaries should be considered.

Fig. 10e shows that the grain boundaries which appear to have moved during grain growth are g-HAGBs. Mobile g-HAGBs are either present in the as-deposited state or form and become mobile due to interaction of ITBs with g-HAGBs. So it is worthwhile to discuss why these g-HAGBs in the multi-twinned microstructure are significantly more mobile than g-HAGBs in sample S1. To this

end, the interactions between a mobile g-HAGB with (a) stationary g-HAGBs and (b) CTBs are addressed in Fig. 12.

The interaction of a stationary g-HAGB attached to a mobile g-HAGB at an arbitrary angle is shown in Fig. 12a. Assuming equal energies for the grain boundaries meeting in the triple junction, it follows that at equilibrium the most favorable angle between the grain boundaries is  $120^\circ$ . Thus, the stationary g-HAGB exerts a drag on the motion of a mobile g-HAGB to bring the junction towards the equilibrium configuration. Then further advancement of the mobile boundary is brought to a halt as indicated by squares on the figure, at time= $t_3$ ). This is the case for the columnar grains of sample S1, where most of the g-HAGBs meet at approximately  $120^\circ$  in the as-deposited state (see Fig. 5), thereby minimizing grain growth.

The interaction of a stationary CTB (shown in grey in Fig. 12b) attached to a mobile g-HAGB at an arbitrary angle is different. At time=0 the energy of boundaries 2 and 3 is equal and since  $\theta_2 + \theta_3 = 180^\circ$ ,  $\sin(\theta_2)=\sin(\theta_3)$ ; Thus,  $\frac{\gamma_2}{\gamma_3} = \frac{\sin(\theta_2)}{\sin(\theta_3)}$ . This is consistent with Young's equation.

Furthermore, the energy of the CTB is significantly lower than the energy of the g-HAGB so  $\sin(\theta_1)\approx 0$  (i.e.  $\theta_1\approx 180^\circ$ ) is also consistent with Young's equation. At time= $t_1$  the HAGB is moved and CTB is extended in length and if  $\theta_1=180^\circ$  the junction is still at equilibrium, because a CTB does not exert a significant drag on the motion of a mobile g-HAGB. This means a microstructure with a high density of CTBs exhibits minor resistance against the motion of mobile g-HAGBs. Fig. 12c and d schematically illustrate the difference between grain growth in a microstructure with low and high density of twin boundaries. It is of importance that in a multi-twinned microstructure, e.g. sample S3, there is a driving force for the annihilation of intrinsic faults, so a mobile g-HAGB advances into the twinned area without a significant drag. Accordingly the high mobility of g-HAGBs in the highly twinned microstructure is not due to the nature of the HAGBs, but is a consequence of the significantly lower drag of twins on their movement. Moreover, the connectivity

of the grain boundaries plays a major role. Twin boundaries that form a unit enclosed by g-HAGBs such as sample S1, Fig. 5, or five-fold twins shown in [33] are more thermally stable as the exterior of the unit (HAGBs) interacts with other HAGBs and protects the interior of the unit composed of twin boundaries, as experimentally observed [28], [33], [34]. This means that the fragmented network of g-HAGBs in a GBE microstructure cannot protect the high density of CTBs and CTBs can be annihilated easily without effective drag of g-HAGBs on the movement of mobile boundaries.

#### ***4.3 Optimal design for high thermal stability***

The thermodynamically stable state of a pure metal is a single crystal with a definite density of vacancies (the number density is a function of absolute temperature) [62]. Accordingly, polycrystalline materials, possessing other defects such as grain boundaries, triple lines, dislocations, etc., have a higher internal energy than the most stable state. Nevertheless, defects in the solid state can enhance the mechanical strength. For the present case, in particular grain boundary strengthening via the Hall-Petch effect appears of importance [63]. This means that optimal design for high thermal stability requires a high density of grain boundaries without compromising the maximum service time/temperature. Considering the properties of different types of grain boundaries [24], [25], CTB has a very low energy and mobility and is the most suitable boundary to achieve high mechanical strength and thermal stability [28], [64]. One could imagine a microstructure which is composed of only CTBs as shown in Fig. 13a. This ideal microstructure for a pure metal is practically impossible to obtain, because ITBs and g-HAGB cannot be avoided. G-HAGBs can be avoided if large scale epitaxial growth is achieved with no nucleation of new crystals; on the other, formation of twin boundaries is dependant on nucleation growth of faulty positioned {111} crystallographic planes (ABCBA stacking instead of ABCAB). The contrasting

requirements of the electrodeposition process results in columnar grains containing twin lamellae, but not the ideal microstructure as shown in Fig. 13a. From a practical point of view, columnar grains and their boundaries are inevitable. Additionally, it was shown for copper that as-deposited nano-twins are inherently defective with kink-like steps and curvature, and the imperfections consist of incoherent segments and partial dislocations [65]. Thus, in practice the incoherent component cannot be fully avoided either and any practically achievable microstructural design must include ITB and g-HAGB.

As discussed above, the incoherent component of a twin boundary is inherent but should be minimal. Comparing samples S1 and S2 shows that a lower ITB fraction increases the thermal stability of twin lamellae. Additionally, the formation of ITB upon annealing must be avoided. Hence, the five-fold junction of twin boundaries (as in sample S3), which inherently has internal strains is unfavorable with respect to thermal stability. It is noted that formation of ITBs is of importance mainly in the early stages of microstructural evolution as by moving and interacting with neighboring boundaries they lose their character. The result of interaction of a  $\Sigma 3$  boundary (ITB in this case) with a g-HAGB is a g-HAGB and when a  $\Sigma 3$  interacts with another  $\Sigma 3$  boundary the result is either a  $\Sigma 1$  (LAGB) or a  $\Sigma 9$  boundary [66]. So, when ITBs interact with their first neighbors they transform to one of the above-mentioned boundaries (g-HAGB,  $\Sigma 1$  or  $\Sigma 9$ ). Accordingly, even in microstructures of high density of twin boundaries, it is the interaction of a mobile g-HAGB with other boundaries that is most important (g-HAGB is either present at as-deposited state and elevated temperatures become mobile or a g-HAGB is the result of interaction of an mobile ITB with a stationary g-HAGB). CTBs that constitute the majority of boundaries lack resistance to the g-HAGB motion, thus, for the optimization of thermal stability, the emphasis should not only be on the high density of CTBs but also on the network of g-HAGB. As indicated earlier, the g-HAGBs of columnar grains are thermodynamically unstable and the only practical

solution to reduce the kinetics of their eventual annihilation is by formation of energy barrier(s). As pointed out earlier, if three g-HAGBs form the  $120^\circ$  configuration, any movement of the triple junction increases the energy in the system, hence, this configuration is an energy barrier which makes the microstructure metastable. For thin samples it is possible to have a columnar grain covering the whole cross-section [67]. In this case, the pinning effects exerted by the deposit free surface and deposit/substrate interface adds to the stability of columns by hindering movement of g-HAGBs.

Accordingly, the optimal microstructure for high mechanical strength and thermal stability is a columnar microstructure in which columnar grain boundaries are of three- $120^\circ$  configuration, see Fig. 13b and c, and also, columnar grains encompass a very high number of CTBs and a very low number of ITBs (there is always ITBs associated with CTBs [65]). The nanotwins of the configuration shown in Fig. 13b are formed because of defects at very early stage of columnar grain formation while the configuration shown in Fig. 13c stems from the repeated faulty positioning of crystallographic planes during deposition. Controlling the twin density of the latter is significantly easier than the former; hence, most of nano twinned microstructures synthesized have the Fig. 13c configuration, which is often credited with being highly thermally stable [68], [28], [65], [69]. Synthesis of nickel electrodeposit with nano-twinned microstructure (Fig. 13c configuration) is successfully carried out by some of the authors. To achieve that,  $\langle 111 \rangle$  fiber texture is necessary which cannot be achieved by simple alteration of pH and current density of electrodeposition and addition of other chemical compounds in the electrolyte is necessary [35]. In addition to the alteration of texture and twin configurations, the columnar grain size significantly decreases. Hence, the microstructure is not comparable to the deposits investigated in this study and more comparable to fully nanocrystalline material. Thermal stability of those will be published elsewhere,

nevertheless, the arguments provided above and the optimal design suggested in this paper are consistent with the experimental study of nano-twinned and nanocrystalline microstructures.

GBE is a powerful tool to enhance material properties and has been employed successfully in combating intergranular failure [70], specially in austenitic steels and nickel based superalloys [71]. Improving thermal stability by GBE is also reported in the literature for austenitic steels, nickel based superalloys and copper [72]–[74], however, the subject has not gained the attention it deserves, yet. The mechanisms of microstructural evolution and optimal microstructural design proposed in this study outlines some important aspects to be considered for engineering FCC material, however, further in-depth studies is required for each material. For austenitic steels and super alloys, the role of alloying elements which is not considered for pure nickel is of particular importance.

### **5. Summary and Conclusions:**

The thermal stability of three nickel electrodeposits with comparable grain size and grain boundary characters, but different fractions of ITBs and their grain boundary networks, were synthesized with varying the electrodeposition conditions. High connectivity of  $\Sigma 3^n$  boundaries significantly lowers the thermal stability. The intrinsic faults in five-fold twin boundary junctions and associated stored energy provide the driving force for the transformation of CTB to highly mobile ITB. Mobile ITBs interact with g-HAGB and form a mobile g-HAGB. There is no significant drag on the motion of a mobile g-HAGB by a stationary CTB. Consequently, g-HAGBs that were present in the as-deposited state become mobile (either because of the elevated temperature or by interaction with a mobile ITB) and can move freely and annihilate the high density of CTB boundaries. Stationary g-HAGBs exert significant drag on the motion of g-HAGBs, hence, a fragmented network of g-HAGB enhances grain growth. An equilibrium configuration of three g-HAGBs meeting with  $120^\circ$  dihedral angles is stable since movement of any of the three increases the energy of the system.

High thermal stability and mechanical strength can be achieved when CTBs are contained within g-HAGBs in three-fold 120° configurations. The density of ITBs must be as low as possible, i.e. must not exceed significantly the density that inherently is associated with CTBs. Additionally the density of crystallographic defects adjacent to CTBs must be low to prevent the evolution of CTB to ITB.

### **Acknowledgement:**

The authors acknowledge the Danish Research Council for Technology and Production Sciences (Grant No. 274-07-0492) for financial support. The A. P. Møller and Chastine Mc-Kinney Møller Foundation is gratefully acknowledged for their contribution toward the establishment of the Center for Electron Nanoscopy in the Technical University of Denmark. Ryutaro Akiyoshi is financially supported by the Strategic Young Researcher Overseas Visits Program from the Japan Society for the Promotion of Science (JSPS). ADR acknowledges support from the U.S. Air Force Office of Scientific Research.

### **References:**

- [1] Y. D. Gamburg and G. Zangari, *Theory and Practice of Metal Electrodeposition*, 2011th ed. Springer, 2011.
- [2] J. Hu, Y. N. Shi, X. Sauvage, G. Sha, and K. Lu, "Grain boundary stability governs hardening and softening in extremely fine nanograined metals," *Science*, vol. 355, no. 6331, pp. 1292–1296, Mar. 2017.
- [3] A. Sharma, S. Chhangani, R. Madhavan, and S. Suwas, "Correlation between crystallographic texture, microstructure and magnetic properties of pulse electrodeposited nanocrystalline Nickel–Cobalt alloys," *J. Magn. Magn. Mater.*, vol. 434, pp. 68–77, Jul. 2017.
- [4] U. Klement, M. da Silva, and G. Hibbard, "Thermal stability of nanocrystalline Ni- and Co-based pulsed current electrodeposits: correlation of calorimetric measurements and microstructure development upon annealing," *Trans. IMF*, vol. 95, no. 1, pp. 20–24, Jan. 2017.
- [5] N. Dong, C. Zhang, J. Li, and P. Han, "Synthesis and Thermal Stability of Nanocrystalline Nickel Coatings by Direct Current Electrodeposition," *Rare Met. Mater. Eng.*, vol. 45, no. 4, pp. 885–888, Apr. 2016.
- [6] M. Hasegawa *et al.*, "Electrodeposition of dilute Ni-W alloy with enhanced thermal stability: Accessing nanotwinned to nanocrystalline microstructures," *Mater. Today Commun.*, vol. 12, pp. 63–71, Sep. 2017.

- [7] T. Niu, W. Chen, H. Cheng, and L. Wang, "Grain growth and thermal stability of nanocrystalline Ni-TiO<sub>2</sub> composites," *Trans. Nonferrous Met. Soc. China*, vol. 27, no. 10, pp. 2300–2309, Oct. 2017.
- [8] V. P. Rangasamy Krishnan and M. Subramanian, "Electrodeposition of Ni-La<sub>2</sub>O<sub>3</sub> composite on AA6061 alloy and its enhanced hardness, corrosion resistance and thermal stability," *Surf. Coat. Technol.*, vol. 324, pp. 471–477, Sep. 2017.
- [9] U. Erb, A. El-Sherik, G. Palumbo, and K. Aust, "Synthesis, structure and properties of electroplated nanocrystalline materials," *Nanostructured Mater.*, vol. 2, no. 4, pp. 383–390, 1993.
- [10] K. Pantleon and M. A. Somers, "X-ray diffraction investigation of self-annealing in nanocrystalline copper electrodeposits," *Scr. Mater.*, vol. 55, no. 4, pp. 283–286, 2006.
- [11] G. D. Hibbard, U. Erb, K. T. Aust, U. Klement, and G. Palumbo, "Thermal stability of nanostructured electrodeposits," in *Materials Science Forum*, 2002, vol. 386, pp. 387–396.
- [12] M. Abdulwahab, O. S. I. Fayomi, A. P. I. Popoola, and M. R. Dodo, "In-situ hybrid study of thermal behaviour of ZnNi and ZnNiAl<sub>2</sub>O<sub>3</sub> nanocrystallite thin films induced TEA/MEA by electrocodeposition," *Results Phys.*, vol. 7, pp. 213–215, Jan. 2017.
- [13] Y. Sun, L. Fu, Z. Fu, A. Shan, and E. J. Lavernia, "Enhanced thermal stability and ductility in a nanostructured Ni-based alloy," *Scr. Mater.*, vol. 141, pp. 1–5, Dec. 2017.
- [14] J. Chen, Y. Zou, K. Matsuda, and G. Zhao, "Effect of Cu addition on the microstructure, thermal stability, and corrosion resistance of Ni-P amorphous coating," *Mater. Lett.*, vol. 191, pp. 214–217, Mar. 2017.
- [15] V. Torabinejad, M. Aliofkhaezaei, S. Assareh, M. H. Allahyarzadeh, and A. S. Rouhaghdam, "Electrodeposition of Ni-Fe alloys, composites, and nano coatings—A review," *J. Alloys Compd.*, vol. 691, pp. 841–859, Jan. 2017.
- [16] Z.-W. Niu and L.-C. Cai, "Ab initio phase stability of some cubic phases of ordered Ni-Fe alloys at high temperatures and pressures," *Comput. Mater. Sci.*, vol. 125, pp. 100–104, Dec. 2016.
- [17] L. Jinlong, W. Zhuqing, L. Tongxiang, K. Suzuki, and M. Hideo, "Effect of tungsten on microstructures of annealed electrodeposited Ni-W alloy and its corrosion resistance," *Surf. Coat. Technol.*, vol. 337, pp. 516–524, Mar. 2018.
- [18] M. H. Allahyarzadeh, M. Aliofkhaezaei, A. R. Rezvanian, V. Torabinejad, and A. R. Sabour Rouhaghdam, "Ni-W electrodeposited coatings: Characterization, properties and applications," *Surf. Coat. Technol.*, vol. 307, pp. 978–1010, Dec. 2016.
- [19] C. C. Koch, R. O. Scattergood, M. Saber, and H. Kotan, "High temperature stabilization of nanocrystalline grain size: Thermodynamic versus kinetic strategies," *J. Mater. Res.*, pp. 1–7, Aug. 2013.
- [20] T. Chookajorn, H. A. Murdoch, and C. A. Schuh, "Design of Stable Nanocrystalline Alloys," *Science*, vol. 337, no. 6097, pp. 951–954, Aug. 2012.
- [21] H. R. Peng, M. M. Gong, Y. Z. Chen, and F. Liu, "Thermal stability of nanocrystalline materials: thermodynamics and kinetics," *Int. Mater. Rev.*, vol. 62, no. 6, pp. 303–333, 2017.
- [22] E. A. Holm and S. M. Foiles, "How Grain Growth Stops: A Mechanism for Grain-Growth Stagnation in Pure Materials," *Science*, vol. 328, no. 5982, pp. 1138–1141, May 2010.
- [23] B. Lin, K. Wang, F. Liu, and Y. Zhou, "An intrinsic correlation between driving force and energy barrier upon grain boundary migration," *J. Mater. Sci. Technol.*, 2017.
- [24] D. L. Olmsted, E. A. Holm, and S. M. Foiles, "Survey of computed grain boundary properties in face-centered cubic metals—II: Grain boundary mobility," *Acta Mater.*, vol. 57, no. 13, pp. 3704–3713, Aug. 2009.
- [25] D. L. Olmsted, S. M. Foiles, and E. A. Holm, "Survey of computed grain boundary properties in face-centered cubic metals: I. Grain boundary energy," *Acta Mater.*, vol. 57, no. 13, pp. 3694–3703, 2009.
- [26] R. Niu, K. Han, Y. Su, T. Besara, T. M. Siegrist, and X. Zuo, "Influence of grain boundary characteristics on thermal stability in nanotwinned copper," *Sci. Rep.*, vol. 6, p. 31410, 2016.
- [27] O. Anderoglu, A. Misra, H. Wang, and X. Zhang, "Thermal stability of sputtered Cu films with nanoscale growth twins," *J. Appl. Phys.*, vol. 103, no. 9, pp. 094322-6, May 2008.

- [28] L. Lu, Y. Shen, X. Chen, L. Qian, and K. Lu, "Ultra-high strength and high electrical conductivity in copper," *Science*, vol. 304, no. 5669, pp. 422–426, Apr. 2004.
- [29] C. A. Schuh, M. Kumar, and W. E. King, "Analysis of grain boundary networks and their evolution during grain boundary engineering," *Acta Mater.*, vol. 51, no. 3, pp. 687–700, 2003.
- [30] T. Watanabe, "Grain boundary engineering: historical perspective and future prospects," *J. Mater. Sci.*, vol. 46, no. 12, pp. 4095–4115, 2011.
- [31] V. Randle, "Special boundaries and grain boundary plane engineering," *Scr. Mater.*, vol. 54, no. 6, pp. 1011–1015, 2006.
- [32] V. Randle and G. Owen, "Mechanisms of grain boundary engineering," *Acta Mater.*, vol. 54, no. 7, pp. 1777–1783, 2006.
- [33] C. Chen, J. Liu, and Z. Wang, "Microstructure stability and evolution in CVD carbonyl Ni materials upon annealing – Grain growth and detwinning process," *Mater. Sci. Eng. A*, vol. 558, pp. 285–297, Dec. 2012.
- [34] A. Kahrmanidis and U. Klement, "Formation of Multiple Twinned Structural Units in Electrodeposited Nickel after Annealing," in *Materials Science Forum*, 2014, vol. 783, pp. 2573–2578.
- [35] H. Alimadadi, A. B. Fanta, M. A. J. Somers, and K. Pantleon, "Crystallographic orientations and twinning of electrodeposited nickel—a study with complementary characterization methods," *Surf. Coat. Technol.*, vol. 254, pp. 207–216, Sep. 2014.
- [36] H. Alimadadi, A. Bastos Fanta, M. A. Somers, and K. Pantleon, "Columns formed by multiple twinning in nickel layers—An approach of grain boundary engineering by electrodeposition," *Appl. Phys. Lett.*, vol. 103, no. 3, pp. 031918–031918, 2013.
- [37] M. Chauhan and F. A. Mohamed, "Investigation of low temperature thermal stability in bulk nanocrystalline Ni," *Mater. Sci. Eng. A*, vol. 427, no. 1–2, pp. 7–15, 2006.
- [38] S. Zaefferer, "On the formation mechanisms, spatial resolution and intensity of backscatter Kikuchi patterns," *Ultramicroscopy*, vol. 107, no. 2–3, pp. 254–266, 2007.
- [39] M. Schaffer, B. Schaffer, and Q. Ramasse, "Sample preparation for atomic-resolution STEM at low voltages by FIB," *Ultramicroscopy*, 2012.
- [40] D. P. Field, "Recent advances in the application of orientation imaging," *Ultramicroscopy*, vol. 67, no. 1–4, pp. 1–9, 1997.
- [41] H. Alimadadi, A. B. Fanta, T. Kasama, M. A. J. Somers, and K. Pantleon, "Texture and microstructure evolution in nickel electrodeposited from an additive-free Watts electrolyte," *Surf. Coat. Technol.*, vol. 299, no. Supplement C, pp. 1–6, Aug. 2016.
- [42] D. G. Brandon, "The structure of high-angle grain boundaries," *Acta Metall.*, vol. 14, no. 11, pp. 1479–1484, 1966.
- [43] T. Wanner, E. R. Fuller Jr., and D. M. Saylor, "Homology metrics for microstructure response fields in polycrystals," *Acta Mater.*, vol. 58, no. 1, pp. 102–110, Jan. 2010.
- [44] T. Kaczynski, K. Mischaikow, and M. Mrozek, *Computational Homology, volume 157 of Applied Mathematical Sciences*. Springer-Verlag, New York, 2004.
- [45] "Computational Homology Project." [Online]. Available: [http://chomp.rutgers.edu/Projects/Computational\\_Homology/OriginalCHomP/software/](http://chomp.rutgers.edu/Projects/Computational_Homology/OriginalCHomP/software/). [Accessed: 15-Jun-2016].
- [46] G. S. Rohrer and H. M. Miller, "Topological characteristics of plane sections of polycrystals," *Acta Mater.*, vol. 58, no. 10, pp. 3805–3814, Jun. 2010.
- [47] H. Alimadadi, A. B. Fanta, and K. Pantleon, "The complementary use of electron backscatter diffraction and ion channelling imaging for the characterization of nanotwins," *J. Microsc.*, 2012.
- [48] J. Notte *et al.*, "An introduction to the helium ion microscope," in *AIP Conference Proceedings*, 2007, vol. 931, pp. 489–496.
- [49] J. Canny, "A computational approach to edge detection," *Pattern Anal. Mach. Intell. IEEE Trans. On*, no. 6, pp. 679–698, 1986.

- [50] A. J. Dammers and S. Radelaar, "Two-dimensional computer modelling of polycrystalline film growth," *Texture Stress Microstruct.*, vol. 14, pp. 757–762, 1991.
- [51] H. Alimadadi, "Grain boundary engineering of electrodeposited thin films," Technical University of Denmark, 2012.
- [52] H. Alimadadi, A. B. Fanta, and K. Pantleon, "The complementary use of electron backscatter diffraction and ion channelling imaging for the characterization of nanotwins," *J. Microsc.*, vol. 249, no. 2, pp. 111–118, 2013.
- [53] J. Amblard, G. Maurin, D. Mercier, and N. Spyrellis, "Structure multimaclee helicoidale autour d'un axe [210] dans les depots electrolytiques de nickel," *Scr. Metall.*, vol. 16, no. 5, pp. 579–584, May 1982.
- [54] E. Snoeck *et al.*, "Quantitative analysis of strain field in thin films from HRTEM micrographs," *Thin Solid Films*, vol. 319, no. 1, pp. 157–162, Apr. 1998.
- [55] V. G. Gryaznov, J. Heydenreich, A. M. Kaprelov, S. A. Nepijko, A. E. Romanov, and J. Urban, "Pentagonal symmetry and disclinations in small particles," *Cryst. Res. Technol.*, vol. 34, no. 9, pp. 1091–1119, 1999.
- [56] D. R. Steinmetz and S. Zaefferer, "Towards ultrahigh resolution EBSD by low accelerating voltage," *Mater. Sci. Technol.*, vol. 26, no. 6, pp. 640–645, 2010.
- [57] H. Alimadadi, A. b. Fanta, and K. Pantleon, "The complementary use of electron backscatter diffraction and ion channelling imaging for the characterization of nanotwins," *J. Microsc.*, vol. 249, no. 2, pp. 111–118, Feb. 2013.
- [58] H. Alimadadi, M. Ahmadi, M. Aliofkhazraei, and S. R. Younesi, "Corrosion properties of electrodeposited nanocrystalline and amorphous patterned Ni–W alloy," *Mater. Des.*, vol. 30, no. 4, pp. 1356–1361, Apr. 2009.
- [59] K. G. Janssens, D. Olmsted, E. A. Holm, S. M. Foiles, S. J. Plimpton, and P. M. Derlet, "Computing the mobility of grain boundaries," *Nat. Mater.*, vol. 5, no. 2, pp. 124–127, 2006.
- [60] H. Alimadadi, A. B. Fanta, T. Kasama, M. A. Somers, and K. Pantleon, "Texture and microstructure evolution in nickel electrodeposited from an additive-free Watts electrolyte," *Surf. Coat. Technol.*, vol. 299, pp. 1–6, 2016.
- [61] I. Adlakha and K. N. Solanki, "Structural stability and energetics of grain boundary triple junctions in face centered cubic materials," *Sci. Rep.*, vol. 5, 2015.
- [62] D. A. Porter, K. E. Easterling, and M. Sherif, *Phase Transformations in Metals and Alloys, Third Edition (Revised Reprint)*. CRC Press, 2009.
- [63] N. Hansen, "Hall–Petch relation and boundary strengthening," *Scr. Mater.*, vol. 51, no. 8, pp. 801–806, Oct. 2004.
- [64] K. Lu, L. Lu, and S. Suresh, "Strengthening Materials by Engineering Coherent Internal Boundaries at the Nanoscale," *Science*, vol. 324, no. 5925, pp. 349–352, Apr. 2009.
- [65] Y. M. Wang *et al.*, "Defective twin boundaries in nanotwinned metals," *Nat. Mater.*, vol. 12, no. 8, pp. 697–702, Aug. 2013.
- [66] V. Randle, "Twinning-related grain boundary engineering," *Acta Mater.*, vol. 52, no. 14, pp. 4067–4081, 2004.
- [67] H. Ma, Y. Zou, A. S. Sologubenko, and R. Spolenak, "Copper thin films by ion beam assisted deposition: Strong texture, superior thermal stability and enhanced hardness," *Acta Mater.*, vol. 98, pp. 17–28, Oct. 2015.
- [68] X. Zhang and A. Misra, "Superior thermal stability of coherent twin boundaries in nanotwinned metals," *Scr. Mater.*, vol. 66, no. 11, pp. 860–865, Jun. 2012.
- [69] X. Zhang, O. Anderoglu, R. Hoagland, and A. Misra, "Nanoscale growth twins in sputtered metal films," *JOM J. Miner. Met. Mater. Soc.*, vol. 60, no. 9, pp. 75–78, 2008.
- [70] T. Liu *et al.*, "Three-dimensional study of grain boundary engineering effects on intergranular stress corrosion cracking of 316 stainless steel in high temperature water," *J. Nucl. Mater.*, vol. 498, pp. 290–299, 2018.

- [71] V. Randle, "Grain boundary engineering: an overview after 25 years," *Mater. Sci. Technol.*, vol. 26, no. 3, pp. 253–261, Mar. 2010.
- [72] L. Tan, K. Sridharan, and T. R. Allen, "Effect of thermomechanical processing on grain boundary character distribution of a Ni-based superalloy," *J. Nucl. Mater.*, vol. 371, no. 1–3, pp. 171–175, 2007.
- [73] K. Kurihara, H. Kokawa, S. Sato, Y. S. Sato, H. T. Fujii, and M. Kawai, "Grain boundary engineering of titanium-stabilized 321 austenitic stainless steel," *J. Mater. Sci.*, vol. 46, no. 12, pp. 4270–4275, 2011.
- [74] S. M. Schlegel, S. Hopkins, and M. Frary, "Effect of grain boundary engineering on microstructural stability during annealing," *Scr. Mater.*, vol. 61, no. 1, pp. 88–91, Jul. 2009.

ACCEPTED MANUSCRIPT

Table 1: Sample names and corresponding electrodeposition conditions.

Sample name	pH	Current density [ $\text{A dm}^{-2}$ ]
S1	4.5	2
S2	4.5	5
S3	2.0	10

**Figure Captions:**

Figure 1: Orientation map color coded in relation with the electrodeposit's growth direction (GD) shown by an arrow in the legend of the cross section of the layers from the layer/substrate interface to the surface; High angle grain boundaries are shown in black; (a) sample S1; (b) sample S2; (c) sample S3;

Figure 2: Ion channeling contrast image obtained on the cross-section of the nickel layer in as-deposited state covering from the substrate to the top surface of samples (a) S1 (b) S2 (c) S3. (d) Higher magnification of a typical region close to the substrate of sample S3.

Figure 3: The square root functions, representing average horizontal intercept length of edge detected images shown in Figure 2 a-c.

Figure 4: Length fraction of  $\Sigma 1$ ,  $\Sigma 3$ ,  $\Sigma 9$  and  $\Sigma 1+\Sigma 3+\Sigma 9$  to all boundaries as a function of distance from the layer/substrate interface for samples (a) S1, (b) S2 and (c) S3.

Figure 5: (a) Ion channeling contrast image of the cross section of sample S1. (b) Top view ion channeling contrast image of the sample S1. (c) 3-dimensional representation of microstructure of sample S1.

Figure 6: A sequence of six ion channeling contrast imaging micrographs (marked 1–6) with an average distance of 70 nm between the sections. Two twin lamellae are marked by red and green dots in the consecutive micrographs.

Figure 7: (a) Development of helical structure from tetrahedra sharing  $\{111\}$  planes, growing parallel to the growth direction. (b) From left to right, two to five face-sharing (also with shared  $\{111\}$  planes) helices. (c) A cross section along an arbitrary plane of five face-sharing helices shown in b. Note the similarity between the model and actual experimental result shown in Fig. 2d.

Figure 8: Ion channeling contrast image of samples (a) S1-673, (b) S2-673 and (c) S3-673. Orientation map color coded in relation with the electrodeposit's growth direction (GD) shown by

an arrow in the legend of the cross section of the layers samples (d) S1-873, (e) S2-873 and (f) S3-873. All high angle grain boundaries are marked in black. The scale bar on the figures in 10  $\mu\text{m}$ .

Figure 9: (a) A low magnification bright field (BF) STEM micrograph of the investigated lamella. (b)-(d) Annular dark field (ADF) STEM images from three different locations marked on (a) by numbers 1, 2 and 3. Some of the jogs at the twin boundary (black arrows) are shown (c). (e) Electron diffraction pattern of the five crystallites shown in (b). (f) Bright field (BF) STEM image obtained at the same location as (b). Strain fields are revealed in BF STEM by darker contrast. (g) BF STEM and the corresponding Fourier-filtered image of the area enclosed by a white square revealing the dislocations.

Figure 10: Experimental evidence of transformation of CTBs to ITBs by comparing before and after annealing. (a) Ion channeling contrast image of sample S3 as-deposited state. (b) Electron channeling contrast image of sample S3-573. (c) TKD image quality map in as-deposited state. (d) TKD image quality map of sample S3-673. Note that (a) and (b) are note the exact same location but comparable regions of the microstructure, however, (c) and (d) are exact same location and grain boundary shown in (c) has curved after annealing. (e) Grain boundary map of the sample S3-673. Two highly curved  $\Sigma 3$  boundaries are marked by green arrows and advancing g-HAGBs are marked by red arrows.

Figure 11: (a) Ion channeling contrast image (b) image quality map of EBSD and (c) orientation map of EBSD of sample S2. Note the higher resolution of ion channeling contrast image and the overlooked twin lamellae in EBSD orientation map.

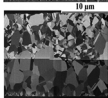
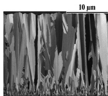
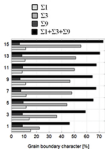
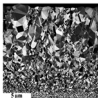
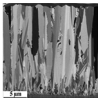
Figure 12: Schematic illustration of (a) Drag exerted by a stationary g-HAGB on the motion of a mobile g-HAGB. The motion is hindered at time= $t_3$  when the three boundaries are at equilibrium. (b) Lack of drag exerted by a stationary CTB (shown in grey) on the motion of a mobile g-HAGB. The CTB extends its length and g-HAGB moves freely. (c) Drag exerted by several stationary g-

HAGBs on the motion of a mobile g-HAGB reduces the kinetics of grain growth. (d) Lack of drag exerted by several stationary CTBs enhances the kinetics of grain growth.

Figure 13: (a) An ideal microstructure composed of only coherent twin boundaries. Optimal microstructure with high population of coherent twin boundaries (green) encompassed by high angle grain boundaries (red) separated by  $120^\circ$ . Twin boundaries are (b) parallel and (c) perpendicular to the growth direction.

## Highlights:

- Three nickel layers of comparable sub-micron grain size and also of comparable density of twin boundaries, but different grain boundary morphology are successfully electrodeposited.
- By annealing nickel electrodeposits at various temperatures, it is found that the density of incoherent twin boundaries and the interaction of mobile grain boundaries with stationary boundaries are the dominant parameters influencing the thermal stability of nickel electrodeposits.
- Based on the detailed experimental results, an optimal microstructural design consisting of coherent twin boundaries and general high angle grain boundaries is proposed to maximize thermal stability of face centered cubic materials with sub-micron grain size.



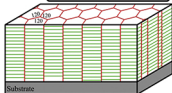
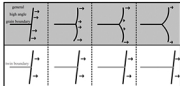
Similar grain boundary character

Electrodeposited Nickel of sub-micron grain size

Different Thermal Stability

Understanding grain boundary interactions

Optimized microstructural design



# Graphics Abstract

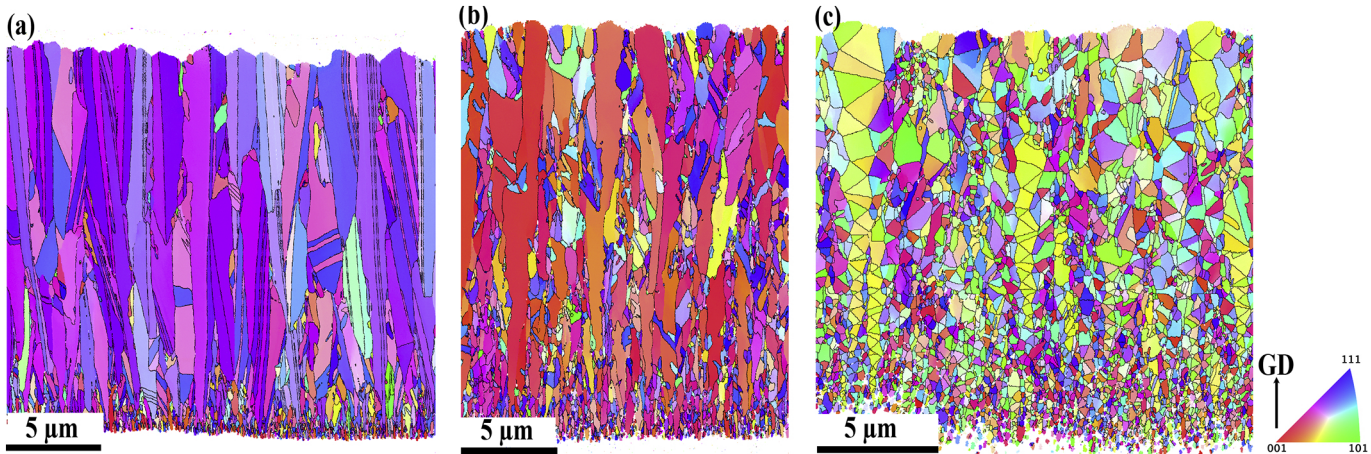


Figure 1

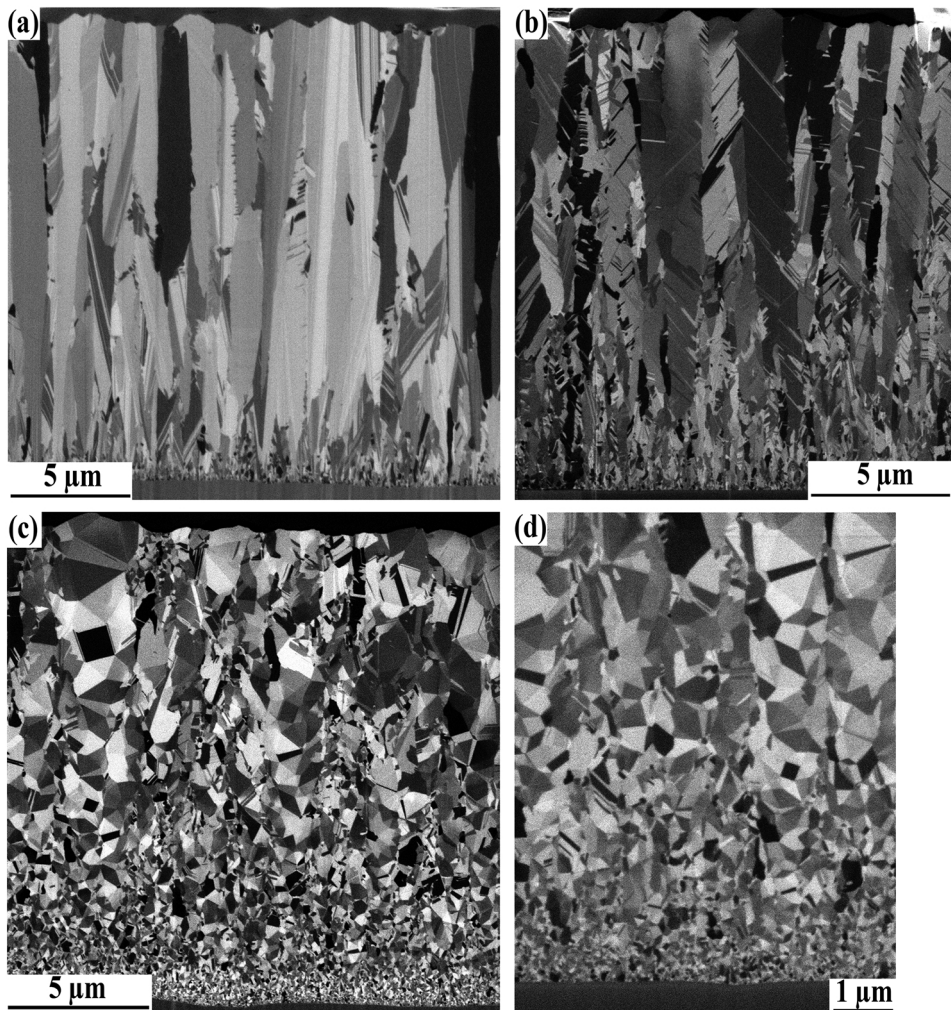


Figure 2

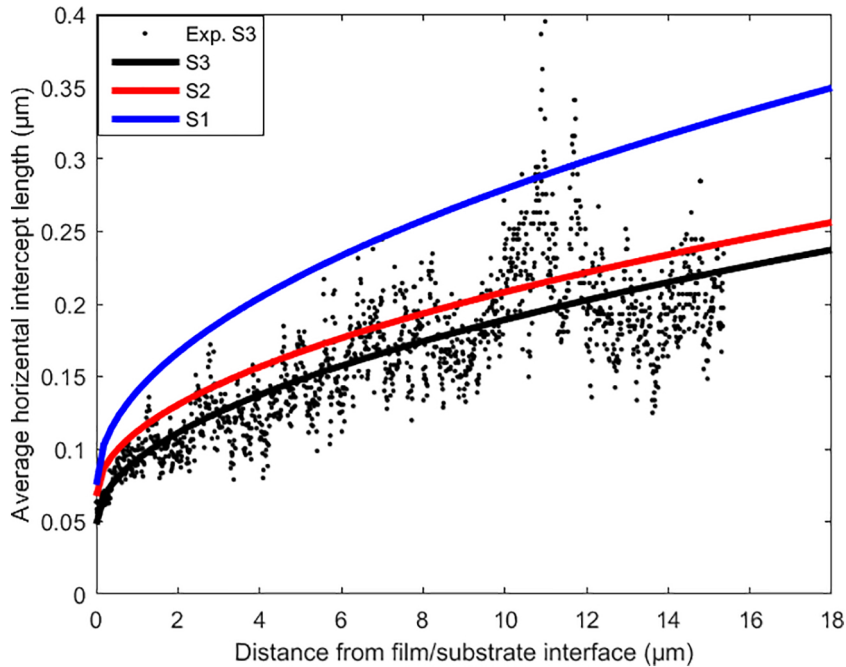


Figure 3

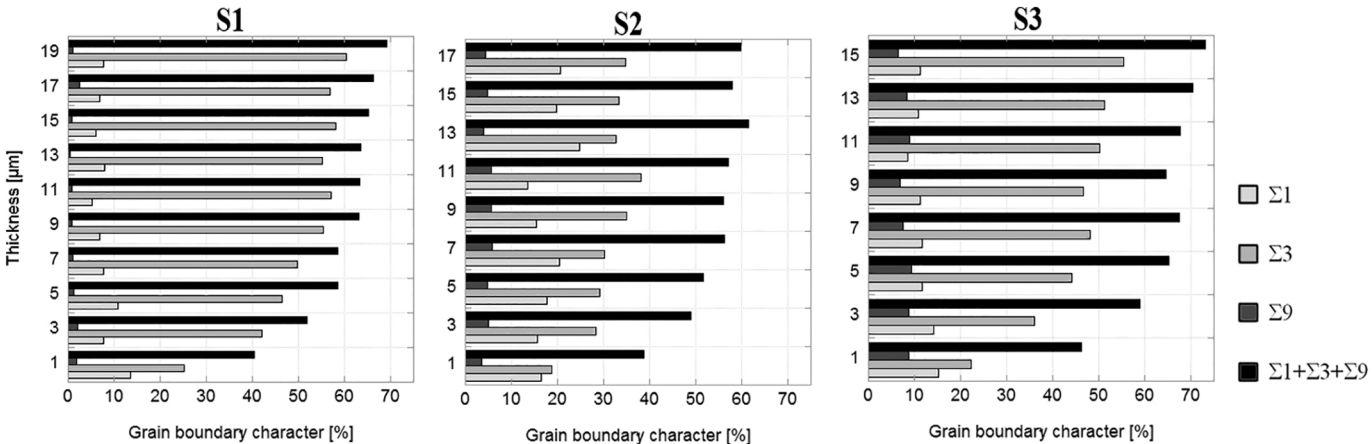


Figure 4

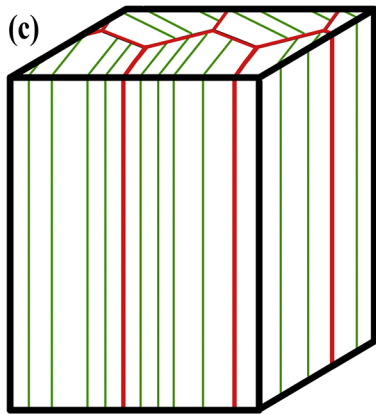
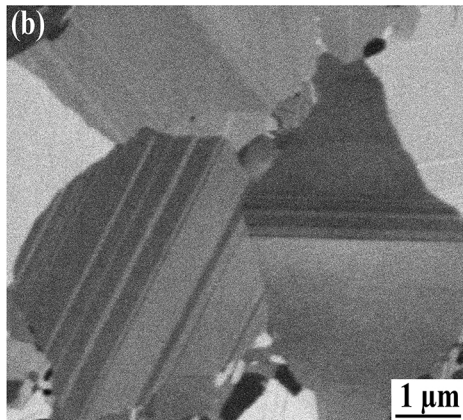
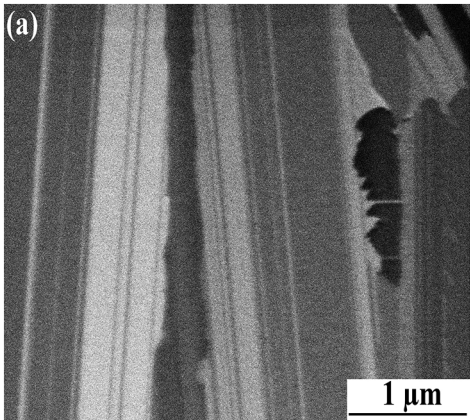


Figure 5

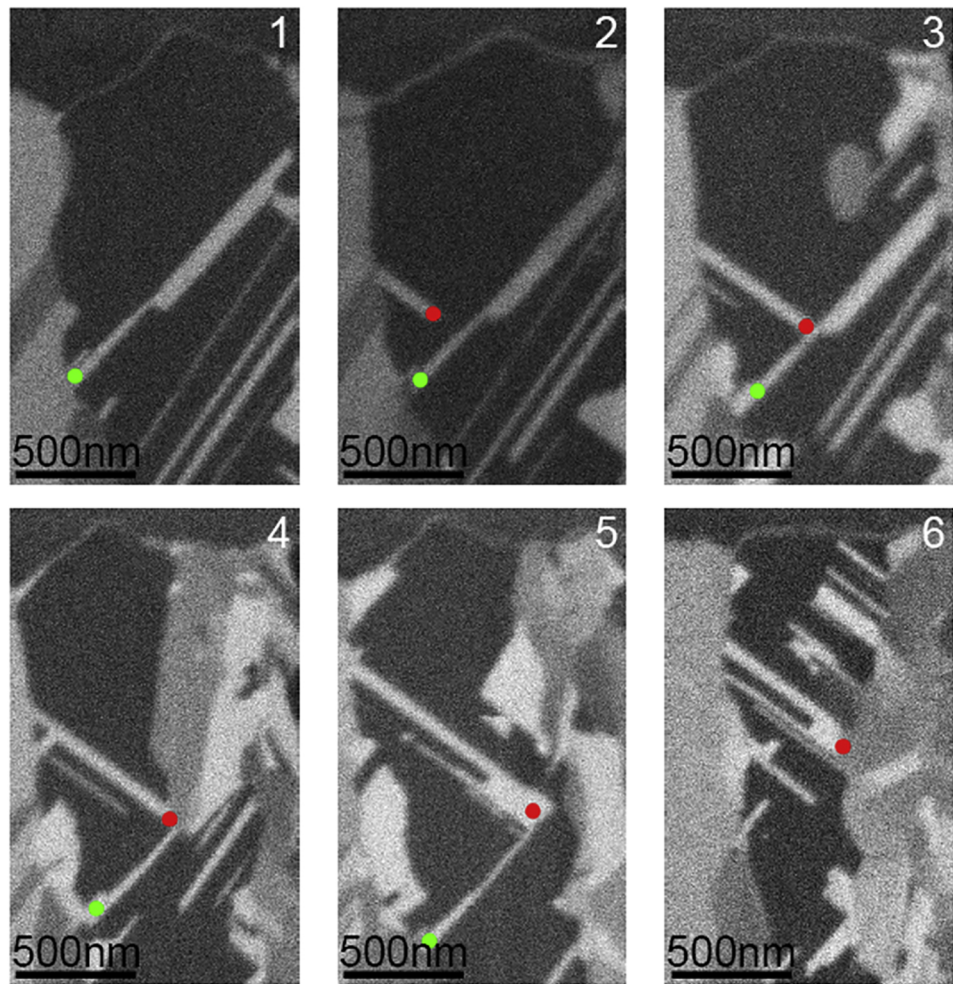


Figure 6

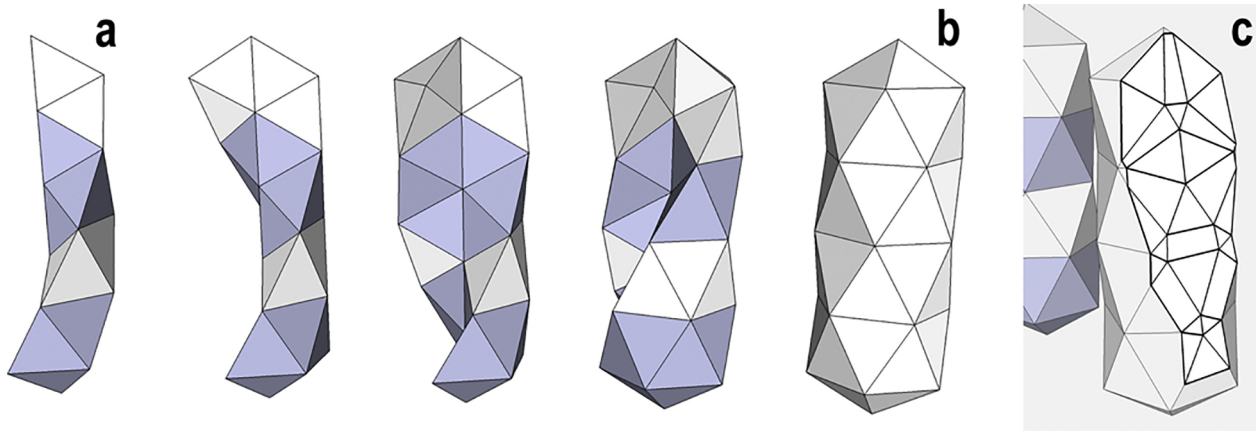


Figure 7

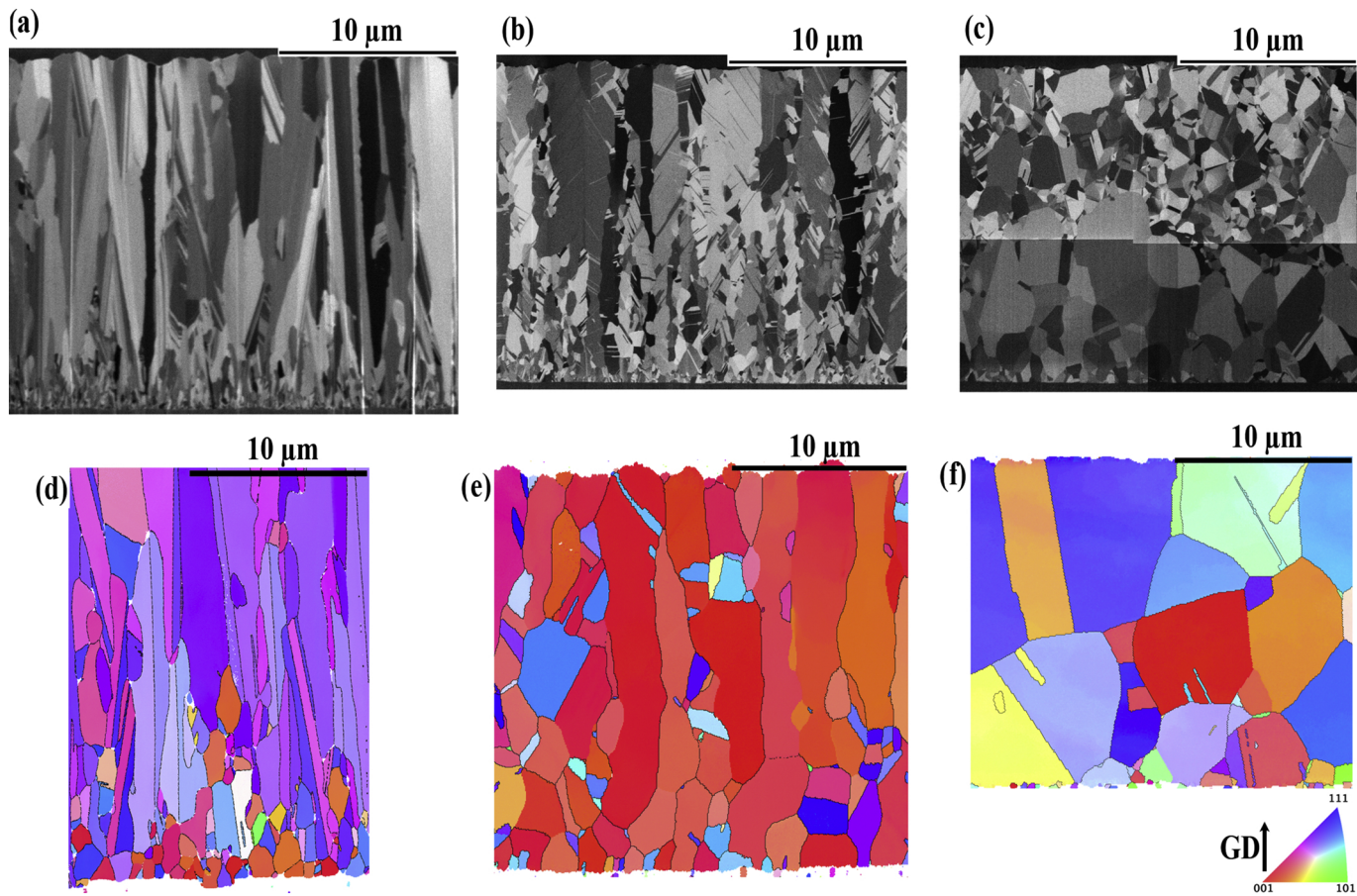


Figure 8

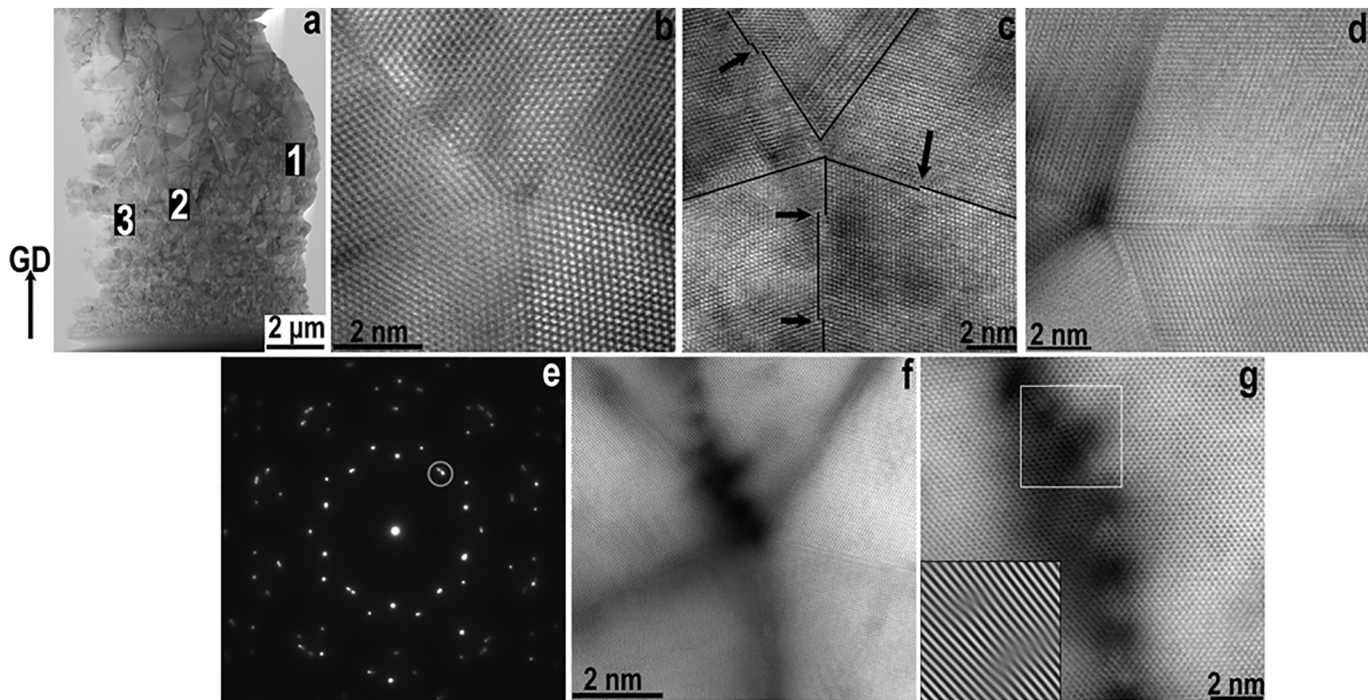


Figure 9

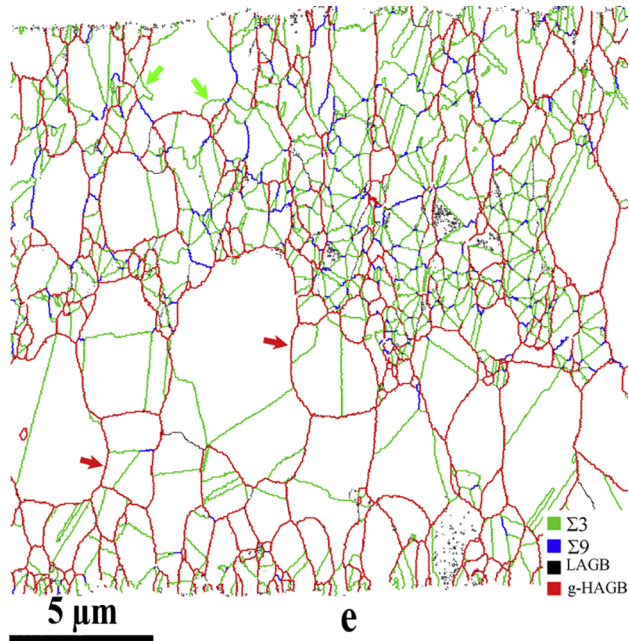
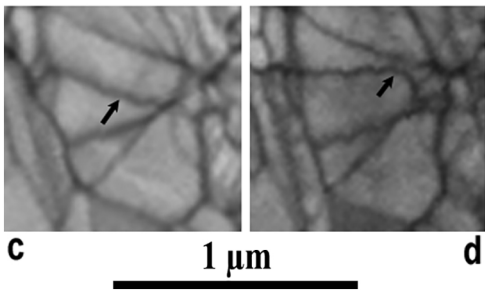
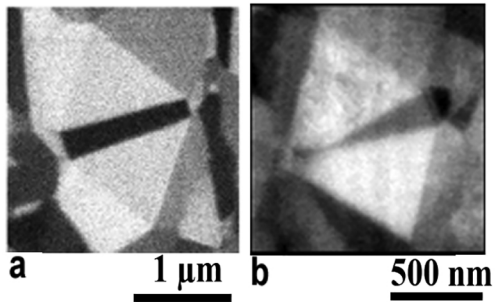


Figure 10

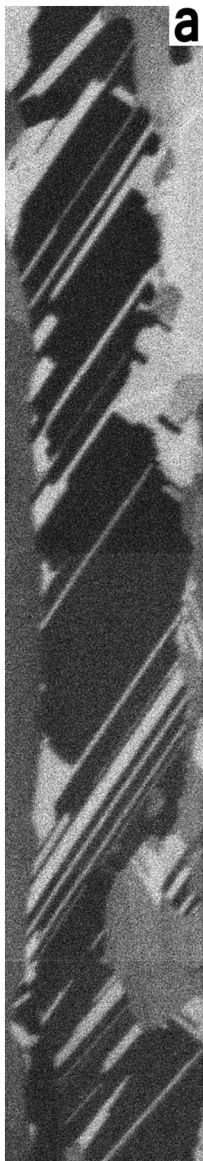


Figure 11

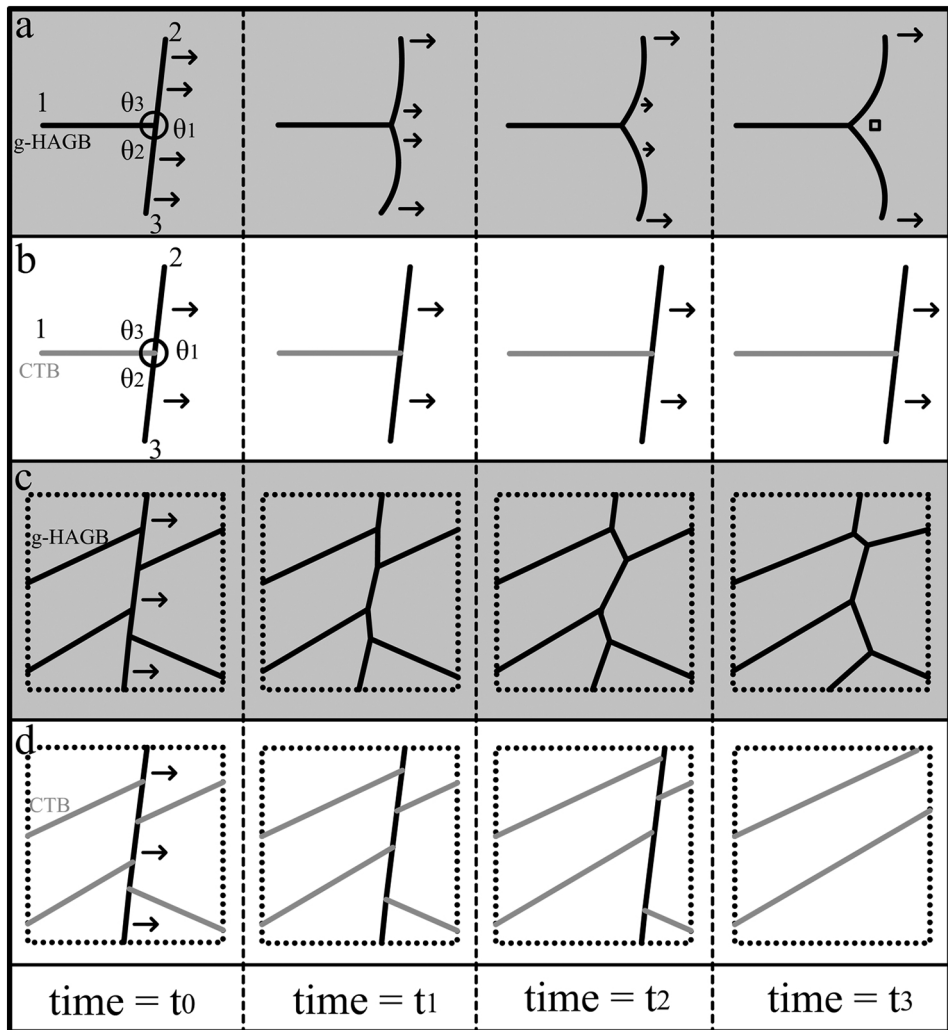


Figure 12

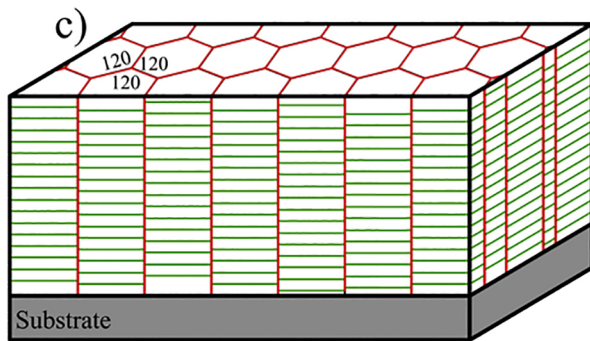
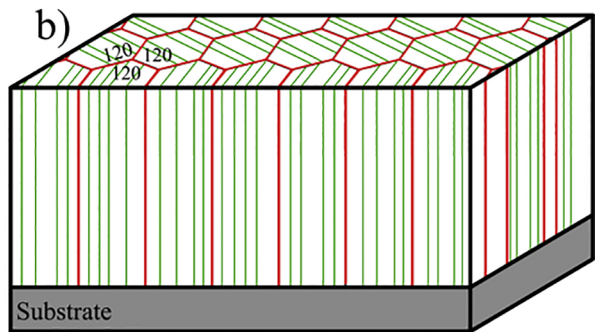
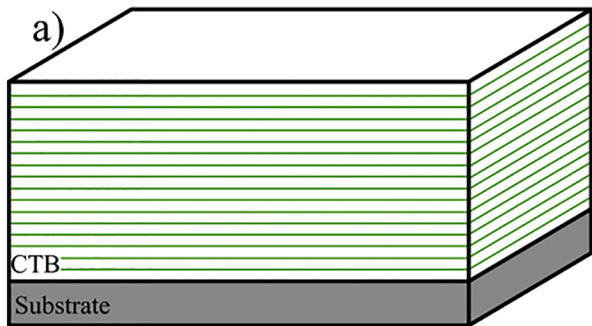


Figure 13